Additive Manufacturing 27 (2019) 606–615

Contents lists available at ScienceDirect

Additive Manufacturing

journal homepage: www.elsevier.com/locate/addma

Full Length Article

Rapid multi-material 3D printing with projection micro-stereolithography using dynamic fluidic control

Daehoon Han[a], Chen Yang[a], Nicholas X. Fang[b], Howon Lee[a,*]

[a] Department of Mechanical and Aerospace Engineering, Rutgers University, New Brunswick, NJ, 08901, USA
[b] Department of Mechanical Engineering, Massachusetts Institute of Technology, Cambridge, MA, 02139, USA

ARTICLE INFO

Keywords:
Multi-material additive manufacturing
Multi-material 3D printing
Projection micro-stereolithography
Multi-functional structure

ABSTRACT

Mask projection stereolithography is a digital light processing-based additive manufacturing technique that has various advantages, such as high-resolution, scanning-free parallel process, wide material sets available, and support-structure-free three-dimensional (3D) printing. However, multi-material 3D printing with mask projection stereolithography has been challenging due to difficulties of exchanging a liquid-state material in a vat. In this work, we report a rapid multi-material projection micro-stereolithography using dynamic fluidic control of multiple liquid photopolymers within an integrated fluidic cell. Highly complex multi-material 3D microstructures are rapidly fabricated through an active material exchange process. Material flow rate in the fluidic cell, material exchange efficiency, and the effects of energy dosage on curing depth are studied for various photopolymers. In addition, the degree of cross-contamination between different materials in a 3D printed multi-material structure is evaluated to assess the quality of multi-material printing. The pressure-tight and leak-free fluidic cell enables active and fast switch between liquid photopolymers, even including micro-/nano-particle suspensions, which could potentially lead to facile 3D printing of multi-material metallic/ceramic structures or heterogeneous biomaterials. In addition, a multi-responsive hydrogel micro-structure is printed using a thermo-responsive hydrogel and an electroactive hydrogel, showing various modes of swelling actuation in response to multiple external stimuli. This new ability to rapidly and heterogeneously integrate multiple functional materials in three-dimension at micro-scale has potential to accelerate advances in many emerging areas including 3D metamaterials, tissue engineering, and soft robotics.

1. Introduction

Additive manufacturing (AM), also referred to as three-dimensional (3D) printing, is a set of manufacturing techniques of directly building 3D physical objects by additively joining raw materials. Since the first invention of AM in 1980's [1], various AM technologies have been developed, such as direct ink writing (DIW) [2,3], fused deposition modeling (FDM) [4], material jetting [5], stereolithography (SLA) [6,7] and two-photon polymerization (2 P P) [8,9]. A variety of materials including polymers [10], metals [11], ceramics [12,13], and biomaterials [14] have been used in AM for a wide range of applications, ranging from rapid prototyping to metamaterials [15,16], medical devices [17], electronics [18], and tissue engineering [19,20]. Although a growing number of materials have become available for AM, most of the existing AM techniques build an object with a single material only, which is a critical barrier to achieving advanced functionalities in 3D printed parts.

Among previously reported multi-material 3D printing techniques, many of them are based on an extrusion-based AM, such as DIW [21–23] and FDM [24,25], or material jetting [26,27]. Since these techniques deposit materials directly to the desired voxel, multi-material printing could be easily implemented by simply adding as many printing nozzles or inkjet heads as the number of materials being processed. However, multi-material 3D printing with a vat polymerization technique such as SLA and 2 P P still remains challenging because an object is built by selectively solidifying a liquid material that is already placed in a vat. To switch a printing material, the whole material in the vat has to be exchanged during the printing, which significantly interrupts and slows down the process, and consequently, increases the overall manufacturing time. In addition, a time-consuming cleaning process between material exchange may be required to remove and rinse out the un-crosslinked material around the object to avoid cross-contamination between materials.

Digital light processing (DLP)-based projection stereolithography

* Corresponding author.
E-mail address: howon.lee@rutgers.edu (H. Lee).

https://doi.org/10.1016/j.addma.2019.03.031
Received 11 February 2019; Received in revised form 21 March 2019; Accepted 26 March 2019
Available online 05 April 2019
2214-8604/

AM has distinctive advantages such as high-resolution, scanning-free parallel process, wide material sets available, low cost, and support-structure-free 3D printing. Among a few recently reported projection stereolithography multi-material 3D printing techniques, the simplest method is to manually change material in the vat [28] or to switch between multiple vats containing different materials [29–31]. However, the printing process has to be stopped for a certain period of time in the middle of the process for material cleaning and change, making the entire production time extremely long. This problem becomes even more apparent when frequent material change is needed for hundreds of layers as material complexity of the part increases. Some groups implemented an automatic material change sequence using a rotational platform where multiple vats for different materials and a cleaning solution were placed [15,32–34]. However, the majority of the production time was still spent on material change because of their long material change time (minutes) compared to the actual time for curing a layer (or curing time, seconds).

Here, we present design and development of a multi-material projection micro-stereolithography (MM-PμSL) system which is capable of rapidly and heterogeneously integrating multiple materials into a 3D structure using dynamic fluidic control of liquid photopolymers within an integrated fluidic cell. The present system can quickly exchange materials without interrupting the process, enabling rapid high-resolution multi-material 3D printing. To achieve this, we characterized material volume flow rate in the fluidic cell, material exchange efficiency, and curing kinetics for various photopolymers with different properties. In addition, we evaluated material cross-contamination occurring during material change to assess the quality of the multi-material printing. Based on the results, we demonstrated 3D printing of a multiple-particle-loaded structure and a multi-responsive hydrogel micro-structure that responds to multiple external stimuli.

2. Materials and methods

2.1. Materials

1,6-Hexanediol diacrylate (HDDA), Poly(ethylene glycol) diacrylate (PEGDA), Acrylic acid (AA), N,N'-Methylenebis(acrylamide) (BIS), Phenylbis(2,4,6-trimethylbenzoyl) phosphine oxide (photo-initiator, PI), Sudan I (photo-absorber, PA), 3,3′-Diethyloxacarbocyanine iodide ($DiOC_2$), Rhodamine B (RhB), Triton X-100 (surfactant), and Phosphate-buffered saline (PBS) were purchased from Sigma-Aldrich. N-Isopropylacrylamide (NIPAAm), Copper (Cu) nano-powder (70 nm), and Alumina (Al_2O_3) powder (BMA 15, 150 nm) were purchased from Fisher Scientific, US Research Nanomaterials, Inc., and Baikowski, respectively. All materials were used as received. Table 1 provides the chemical components of the solutions used in each study and their concentrations.

2.2. Multi-material projection micro-stereolithography (MM-PμSL) system

The MM-PμSL system was built with the following major components: a UV LED (405 nm, Innovations in Optics), custom-built collimation optics (Thorlabs), a beam splitter (Thorlabs), a digital dynamic mask (liquid crystal on silicon, LCoS) extracted from a commercial digital projector (Cannon), a projection lens (Carl Zeiss), a linear stage (Newport Corporation), a custom-built fluidic cell, a pump (Parker), and 2-way pinch valves in each fluidic path (Reet Corp.). The fluidic cell consists of a cylindrical printing chamber with integrated microfluidic inlet and outlet channels, a cylindrical build platform with an embedded pumping channel, and a top plate with a circular hole to clamp a glass/PDMS window. Detailed drawings of each component and assembly is included in Fig. S1 (Appendix A). In this study, we used 3 material containers for 3 different materials, but it can be easily extended for as many materials as needed. All components of the system are controlled by a custom-written LabVIEW (National Instruments) script.

2.3. Fluid flow measurement in MM-PμSL

In order to measure a volume flow rate of a liquid material in the MM-PμSL system, a material container was first connected to the fluidic cell. After filling in the container with the material to be tested, we started the pump to create a pressure-driven flow through the fluidic cell. The material discharged from the outlet of the pump for a given pumping time was collected and weighed using a digital balance. Discharged volume was calculated using a density of the material (Table 2).

2.4. Viscosity measurement

Viscosity of four different materials, namely, ethanol, HDDA, PEGDA 250, and PEGDA 575, was measured at room temperature by viscometer (DV-II + Pro, Brookfield Engineering Lab) with a cone-and-plate geometry (Table 2). 1 mL of each material was loaded between a cone with 48 mm diameter and a plate, and a shear stress was measured to calculate the viscosity. A shear rate of 20 rpm was used for all materials.

2.5. Fluorophore concentration measurement using a plate reader

Fluorescent intensity of $DiOC_2$ solutions were measured using a plate reader (Infinite M200 Pro, Tecan). Fluorescence filters with an excitation wavelength of 482 nm and an emission wavelength of 513 nm were used. 100 μL of sample fluorescent solutions were pipetted into the wells of a standard 96-well plate. The fluorescent intensity was measured from the bottom of the plate. Fluorophore concentration of $DiOC_2$ solutions were calculated using the calibration curves showing the relationship between fluorophore concentration and fluorescent intensity (Appendix A. Fig. S2). To obtain the calibration curves, five solutions with predetermined fluorophore concentrations (0, 0.1, 0.2, 0.4, and 0.8 μM) were prepared and the intensity of each solution was measured using a plate reader.

2.6. Fluorescent microscope imaging for cross-contamination study

Imaging of the printed structures containing fluorophores was performed using an inverted fluorescent microscope (IX81, Olympus). To quantify the degree of material cross-contamination in a printed sample, green and red fluorescent microscope images of the sample were individually taken with two different filters. The green and red fluorescent intensities were extracted along a line at the center of the image (Appendix A. Fig. S3a) using image analysis software, Image J. Then the obtained intensities were normalized to their respective maximum intensity (Appendix A. Fig. S3b for green and Fig. S3c for red). The area under each peak was calculated using data analysis software, Origin and *cross-contamination index* and *purity index* were determined based on these areas (see section 3.5 for details).

2.7. Confocal fluorescent microscope imaging

A sample to be imaged was tightly attached to a glass slide using super glue. The glass slide on which the sample was placed was put on the inverted laser scanning confocal microscope (LSM 780, Zeiss). The green and red confocal fluorescent microscope images of the sample were individually taken with two different filters, and then two separate images were analyzed and merged using image analysis software, Image J.

2.8. X-ray micro computed tomography (CT) imaging

The 3D printed multi-material helix in Fig. 4(d) was prepared inside

Table 1
Material composition of different printing solutions. Ethanol was used as a solvent for NIPAAm solution.

Study	Material composition							
	Monomer (M)	Cross-linker (mM)	PI (mM)	PA (mM)	$DiOC_2$ (μM)	RhB (μM)	Particles (vol. %)	Triton X-100 (mM)
Flow control (Sec.3.2)	Ethanol (control)	–	–	–	–	–	–	–
	HDDA	–	–	–	–	–	–	–
	PEGDA250	–	–	–	–	–	–	–
	PEGDA575	–	–	–	–	–	–	–
Material exchange process (Sec.3.3)	Ethanol (control)	–	–	–	0.8	–	–	–
	HDDA	–	–	–		–	–	–
	PEGDA250	–	–	–		–	–	–
	PEGDA575	–	–	–		–	–	–
Curing kinetics (Sec. 3.4)	PEGDA250	–	47.8	–	–	–	–	–
		–		–	0.8	–	–	–
		–		–	–	0.8	–	–
		–		–	1000	–	–	–
		–		–	–	1000	–	–
		–		–	–	–	Cu (0.45)	3.2
		–		–	–	–	Al_2O_3 (0.45)	3.2
Cross-contamination (Sec.3.5)	PEGDA250	–	47.8	–	0.8	–	–	–
		–		–	–	0.8	–	–
Multi-material 3D micro-structures (Sec.3.6.1)	PEGDA250	–	47.8	–	1000	–	–	–
		–		–	–	1000	–	–
Multi-particle-loaded structure (Sec.3.6.2)	PEGDA250	–	47.8	–	–	–	–	–
		–		–	–	–	Cu (0.45)	3.2
		–		–	–	–	Al_2O_3 (0.45)	3.2
		–		–	–	–	Cu (16)	3.2
		–		–	–	–	Al_2O_3 (16)	3.2
Multi-responsive hydrogel structure (Sec.3.6.3)	NIPAAm (6.2)	BIS (324)	47.8	12	–	–	–	–
	AA (13.3)	PEGDA250 (404)	47.8	–	–	–	–	–

Table 2
Material properties of liquid material samples.

Property	Ethanol	HDDA	PEGDA 250	PEGDA 575
Viscosity (cP)	1	6.3	13.4	58.7
Density (kg m^{-3})	782	1,010	1,110	1,120

a pipette tip to immobilize the structure. The tip was, then, placed on the sample holder in the Skyscan 1172 Micro-CT system (Bruker). The structure was scanned at a resolution of 6.5 μm. Afterwards, the cross-sectional images were used to reconstruct a 3D image of the structure with the Skyscan image reconstruction software, NRecon.

2.9. Multi-responsive hydrogel swelling experiment

The bilayer hydrogel beam in Fig. 5 was printed using MM-PμSL with two different hydrogels, a thermo-responsive hydrogel and an electroactive hydrogel. After printing, the sample was stored in DI water overnight for rinsing. Then the sample was put into a 0.05 M PBS solution and stored at 5 °C for 24 h. To test responsive swelling with varying temperature and electric field, the bilayer hydrogel beam was placed between two platinum wire electrodes separated by 5 cm in a temperature-controlled chamber filled with 0.05 M PBS solution. After setting the temperature, an electric field was applied for 10 s using a DC power supply (voltage of 30 V). In order to let it return to its original shape, the sample was left in the chamber at the same temperature for 10 min with no electric field applied. The reverse electric field was then applied for 10 s at the same electric field strength. All deformations of the sample were recorded with a digital camera.

3. Results and discussion

3.1. MM-PμSL system and process overview

Projection micro-stereolithography (PμSL) is a high-resolution vat polymerization AM technique which uses a digital micro display as a dynamic mask generator [30,35–41]. As shown in Fig. 1a, a 3D model created by computer aided design (CAD) software is digitally sliced into a series of cross-sectional images. Ultraviolet (UV) light from a UV light emitting diode (LED) is first guided to the dynamic mask generator which displays a digital image. Then, the spatially patterned UV light is projected through a projection lens and focused on the surface of a liquid photopolymer. Upon UV exposure, the liquid photopolymer is converted to solid, rapidly forming a layer in a desired pattern in seconds. Then the build platform on which a printed object sits is lowered vertically, and the next image is projected to form a new layer on the proceeding one. This process is repeated for all the layers until the 3D object is completed. PμSL is compatible with a variety of photopolymers including shape memory polymers [30,42] and hydrogels [39,40,43]. Metal and ceramic 3D printing has been also achieved through PμSL by using metallic [15] and ceramic [41] particles suspended in a liquid photopolymer solution or using polymer-derived ceramics [44].

In this work, we present a multi-material PμSL system that can rapidly switch photocurable materials. To achieve quick and active material exchange, we designed and fabricated an integrated pressure-tight fluidic cell in place of an open vat. Schematic diagram of the system is shown in Fig. 1a. A transparent glass window coated with polydimethylsiloxosane (PDMS) is tightly clamped to the top of the fluidic cell. Being optically transparent, the PDMS coating allows the UV light ($\lambda = 405$ nm) to pass through and reach a photocurable polymer solution in the fluidic cell. Oxygen permeability of PDMS helps to create a thin inhibition layer at the PDMS-photopolymer interface, facilitating separation of a polymerized layer from the PDMS when the printing platform is lowered for the next cycle [45,46]. In addition, elastic PDMS coating serves as a gasket, ensuring tight sealing of the fluidic cell to prevent material leaking or gas bubble forming during the pressure-driven material exchange process. Multiple UV-protected material containers and a pump are connected to the fluidic cell through tubing and internal fluidic channels of the fluidic cell. Through a computer-controlled valve and pump operation sequence, the fluidic cell is filled with a material to be printed. When material change is

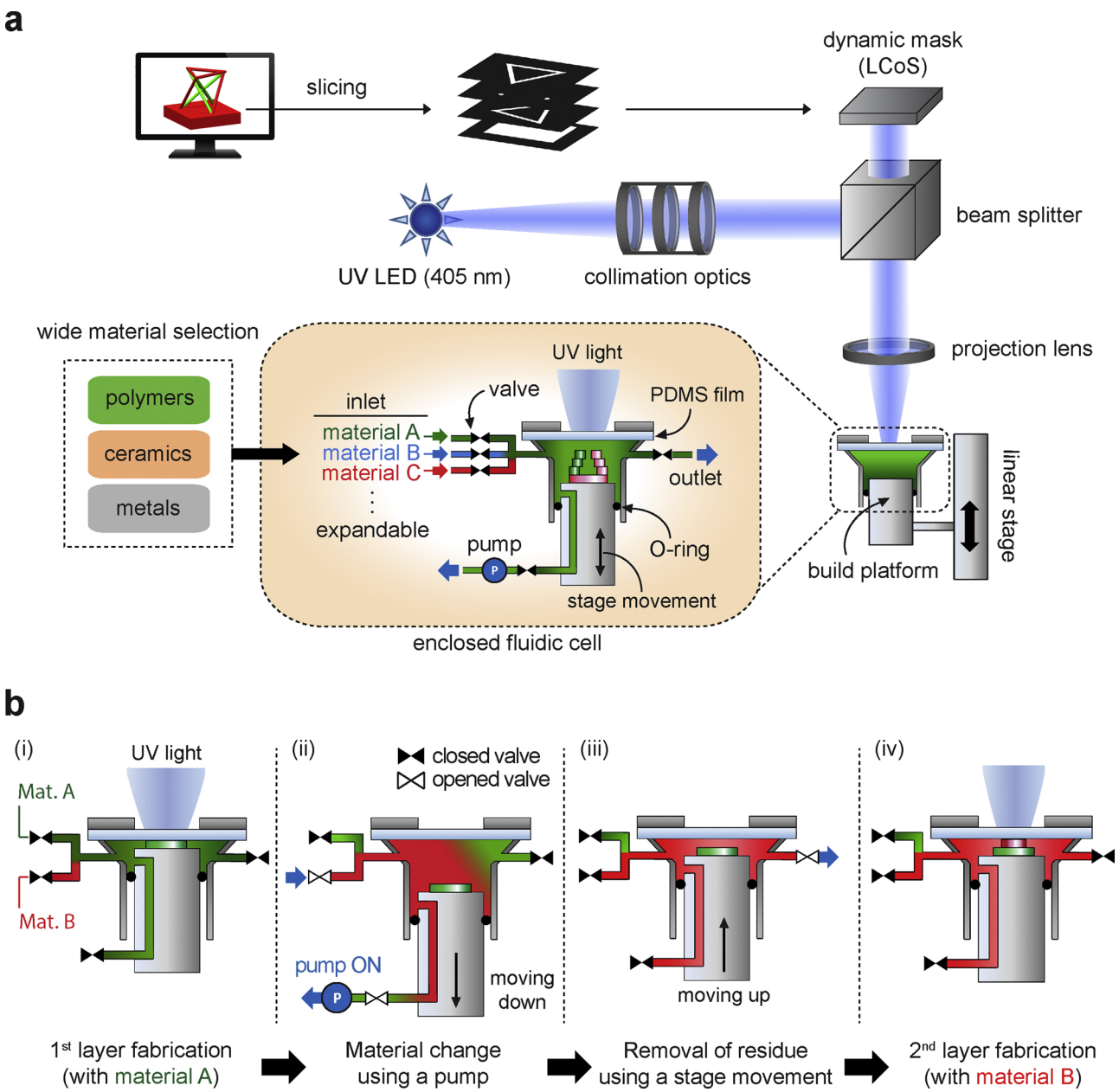

Fig. 1. Schematic illustration of the MM-PμSL overall process (a) and material exchange process (b).

needed, a new material in a respective container is quickly pumped to the fluidic cell to replace the previous material in the printing chamber (Appendix B. Video S1). Once the chamber is completely filled with a liquid material in the beginning, no air bubble that could scatter projection light is generated inside the fluidic cell because of the tight sealing achieved by elastic PDMS coating. The custom-built multi-material PμSL system is shown in Fig. S1 (Appendix A). With the current configuration, the optical system can deliver light irradiance of up to 200 $mWcm^{-2}$ with a lateral resolution of 5 μm on the projection plane.

Fig. 1b illustrates the material exchange process. A material in the fluidic cell is replaced by a pressure-driven flow of a new material. The following sequence is to change the printing material from material A (green) used for the previous layer (i in Fig. 1b) to material B (red) for the subsequent layer. First, the valve for material B opens when the build platform moves down. This process creates a negative pressure inside the fluidic cell, driving the flow of material B into the fluidic cell. Once the platform completes descending, the pump connected to the fluidic cell through the center channel is turned on to flush the fluidic cell with material B while drawing the remaining material A out of the fluidic cell (ii in Fig. 1b). While doing so, the structure being printed on the build platform in the fluidic cell is vigorously rinsed with material B, eliminating the need for a separate cleaning process which would be otherwise necessary to remove uncured material around the structure. When material change is completed, the pump is turned off, and the build platform pushes the residual material through the outlet channel of the fluidic cell while moving up to the position for the next layer (iii in Fig. 1b). Then, the outlet channel of the fluidic cell is closed, leaving the fluidic cell now filled with material B for the next layer to be cured on top of or next to the previous layer upon UV exposure (iv in Fig. 1b). Not only can this process build layers of different materials on top of each other, it can also integrate different materials side-by-side within the same layer. By performing this automated process whenever material change is necessary, different materials can be three-dimensionally (vertically and horizontally) joined together, resulting in a true multi-material 3D object.

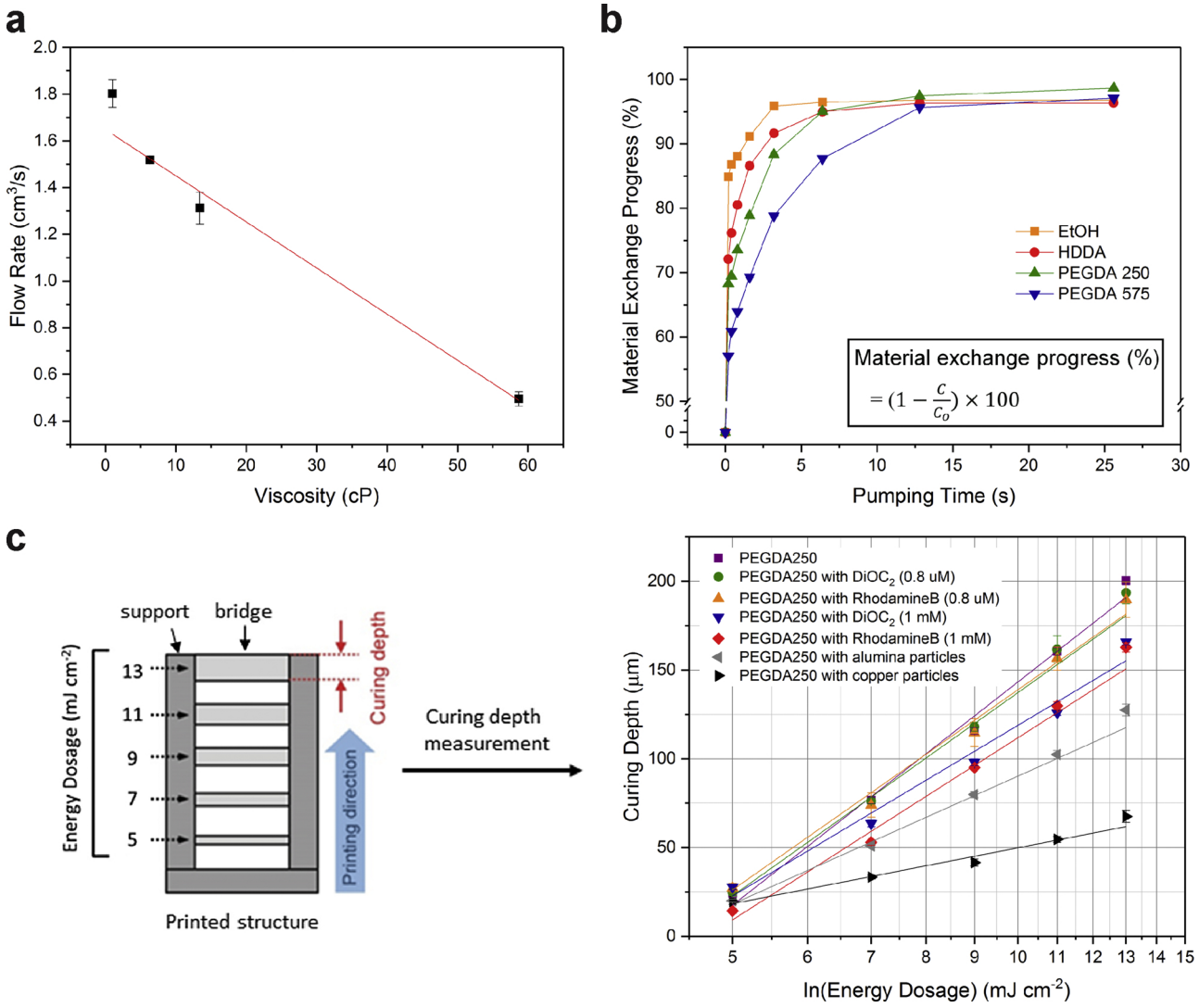

Fig. 2. MM-PμSL system characteristics. (a) The relationship between viscosity and material flow rate in the fluidic cell. (b) Time evolution of material exchange progress for four different materials, namely ethanol (orange squares), HDDA (red circles), PEGDA 250 (green triangles), and PEGDA 575 (blue inverted triangles). (c) MM-PμSL curing depth working curves for different materials. The curing depth increases with energy dosage, but shows different growth rates depending on material. (For interpretation of the references to colour in this figure legend, the reader is referred to the web version of this article).

3.2. Flow control in the fluidic cell for material change

In the material change process described above, the time required for the material to be completely replaced varies depending on the volume flow rate, which is closely related to the viscosity of the material when an applied pressure is given [47]. Since different liquid feedstock materials may have different viscosity, the relationship between the viscosity of the material and the material flow rate through the fluidic cell can help to predict the minimum material exchange time required. For this study, we used four different liquid material samples with different viscosity, namely ethanol, HDDA, PEGDA 250, and PEGDA 575 (Table 2) and measured their respective flow rates during pumping. As shown in Fig. 2a, the average flow rate of ethanol, HDDA, PEGDA 250, and PEGDA 575 is 1.8, 1.5, 1.3, and 0.5 $cm^3\ s^{-1}$, respectively. With any of these volume flow rates, the fluidic cell having an internal chamber volume of ~1 cm^3 can be filled in a matter of seconds. The result shows that viscosity and volume flow rate are inversely proportional, as predicted by Hagen-Poiseuille law [47]. Since different materials would need different material change times, the overall printing time to complete a multi-material 3D structure can be minimized by giving a material exchange time tailored to the viscosity of the material being processed.

3.3. Material change process

For a given flow rate, a longer pumping process introduces a higher volume of a new material into the fluidic cell, leading to more thorough material exchange. At the same time, it increases overall printing time and material consumption. Therefore, it is important to determine an appropriate pumping time for given materials to maximize process throughput and material efficiency. To determine a pumping time, evolution of material composition in the fluidic cell during the material exchange process was measured. To this end, the fluidic cell was first filled with a liquid material sample (ethanol, HDDA, PEGDA 250, or PEGDA 575) containing 0.8 μM of green fluorescent dye ($DiOC_2$). The concentration of the fluorescent dye was constantly monitored while the same material without a dye was driven into the fluidic cell. As material exchange progresses, the material in the fluidic cell is diluted and concentration of the dye decreases. We sampled the solution from the fluidic cell at 0.2, 0.4, 0.8, 1.6, 3.2, 6.4, 12.8, and 25.6 s of pumping time, and measured the fluorescent intensity by a plate reader (Infinite M200 Pro, Tecan) (λ_{ex}: 482 nm, λ_{em}: 513 nm). Then, we calculated the

fluorophore concentration with calibration curve (Appendix A. Fig. S2) showing the relationship between fluorophore concentration and fluorescent intensity (see Materials and Methods for details). Material exchange progress was quantitatively assessed with the fluorophore concentrations (Fig. 2b). We define *material exchange progress index* (%) as $\left(1-\frac{c}{c_0}\right)\times 100$, where c and c_0 are current and initial concentrations of the fluorescent dye in the fluidic cell. Fig. 2b shows time evolution of material exchange progress indices for all tested materials. If we set the threshold material exchange progress to be 95%, material exchange times for ethanol, HDDA, PEGDA 250, and PEGDA 575 are 3.2, 6.4, 6.4, and 12.8 s, respectively. It is clearly seen that more viscous material requires more time to complete material exchange because of low volume flow rate. However, even with PEGDA 575 having a relatively high viscosity of 65 cP, near complete material exchange can occur within around 10 s. Compared to previously reported works (Wang et al. [15] and Zhou et al. [33]), our multi-material process using dynamic flow control offers more than 30 times faster material switching, while maintaining exceptional printing resolution inherited from PμSL. The smallest feature size achieved with this system is 5 μm (Appendix A. Fig. S4), which is more than an order of magnitude better than the reported multi-material stereolithography techniques (300 μm, Wang et al. and Zhou et al.).

3.4. Curing kinetics of different photopolymers

When a layer is formed upon light irradiation, photopolymerization starts from the top surface of the photopolymer and propagates into the polymer, resulting in continuous growth of the layer thickness over time. This thickness is called curing depth [48]. Since different photopolymers or the same photopolymer with different precursor or dye concentrations may have different reactivity, different light energy should be given to keep the layer thickness constant across multiple materials. To study the effect of light energy dosage on curing depth, we prepared a set of liquid photopolymers as listed in Table 1. A test structure comprised of two side supports and five suspended bridges between the supports was printed for each photopolymer (Fig. 2c). A sufficient vertical distance between the bridges (240 μm) was given such that the bridges were not touching with each other. Due to different levels of energy dosage given, each bridge grew to a different thickness. The intensity of UV light was 10.0 mW cm^{-2}, and exposure time for the bridges gradually increased from 0.5 to 1.3 s in increments of 0.2 s. Thickness of the bridges was measured using an optical microscope, and the curing depth as a function of light energy dosage was plotted for different photopolymer solutions in Fig. 2c. The curing depth increases with energy dosage, but at a different rate depending on material, following the stereolithography working curve equation, $C_d = D_p \ln(E/E_c)$, where C_d is a curing depth, and E is a light energy. Two key constants of a liquid photopolymer, D_p and E_c, are characteristic cure depth and critical energy, respectively [48]. Curing time per layer for a given material and for a desired layer thickness was determined based on this result. Table 3 lists all process parameters used to fabricate the multi-materials samples presented in the following sections.

3.5. Cross-contamination between materials

Since the material in the fluidic cell is gradually changed as a new material flows in, the material being replaced can be left behind in the fluidic cell if an influx of a new material is insufficient. In this case, a mixture of the two materials is present in the fluidic cell during crosslinking, which reduces a contrast between different materials, thereby degrading distinctive property and functionality of each material as well as the print quality of the multi-material structure. We call this cross-contamination. To achieve high-quality and high-fidelity multi-material 3D printing, we evaluated the effect of material exchange time on cross-contamination. Three identical test structures shown in Fig. 3a were printed with PEGDA 250-based photopolymer solutions (Table 1) using different material exchange times of 3, 7, and 11 s. The test structures have four thin strips (100 μm) made of two different fluorescent materials (Table 1). The 2nd and 4th strips were printed with the green material, followed by material switch to the red material for the 1st and 3rd strips, as illustrated in Fig. 3a. The green and red fluorescent images of the structure were taken using a fluorescent microscope (Fig. 3b and Appendix A. Fig. S3a) and intensity for each color was extracted from the image to quantify a degree of material cross-contamination in a printed sample. The obtained intensities were normalized to their respective reference intensity (Appendix A. Fig. S3b for green and Fig. S3c for red). Since the 2nd and 4th green strips were first printed without any foreign materials present, their green intensity is constant regardless of the pumping time, and it can be considered as the intensity of a pure green material (reference green intensity) (Appendix A. Fig. S3b). Therefore, we defined *cross-contamination index* as a ratio of undesirable green intensity present in the red strips (1st and 3rd) to the reference green intensity from the green strips (2nd and 4th). On the other hand, *purity index* is defined as a ratio of red intensity measured from the red strips (1st and 3rd) normalized to the reference red intensity taken from the sample with the maximum red intensity (11-s sample) (Appendix A. Fig. S3c). The mixed colors representing significant cross-contamination between the two materials were observed in the red strips (1st and 3rd). These mixed colors are most apparent in the 3-s sample. As material exchange progresses, cross-contamination index decreases from 1 to 0, while purity index increases from 0 to 1. Note that the sum of these two indices is not necessarily one because they are based on different reference values. Fig. 3c plots progression of the two indices with pumping time, showing that increasing material influx during material change process will result in a high material contrast in a multi-material structure with low cross-contamination. However, it is worth noted that prolonged pumping time will eventually slow down overall printing process and increase material consumption. The material consumption during 11 s pumping (14 cm^3) was about 1.6 times higher than 7 s pumping (9 cm^3). In all subsequent experiments using PEGDA 250-based photopolymer solutions, a material exchange time of 7 s was used.

3.6. Rapid, high-resolution multi-material 3D printing

3.6.1. Multi-material 3D micro-structures

Using the MM-PμSL system and multiple photocurable materials (Table 1), we printed 3D micro-structures as shown in Fig. 4a–c. First, a Taiji symbol patterned cylindrical structure was printed (Fig. 4a). The diameters of the whole structure and the small dot inside are 1 mm and 100 μm, respectively. Two distinctive colors with clear boundaries were observed. We also fabricated a tensegrity structure consisting of high aspect ratio beams with different materials as shown in Fig. 4b. The diameter of the struts is 100 μm and the height of the overall structure is 2 mm. Fluorescent microscope images clearly show that the structure was created with two different materials (green and red). Third, we printed a bilayer micro-capillary structure with a hollow channel (inner diameter of 100 μm) as shown in Fig. 4c. Each layer has a thickness of 50 μm, which is clearly seen from the confocal fluorescent microscope images in different parts of the structure: top (Fig. 4c(ii)), middle (Fig. 4c(iii)), and bottom (Fig. 4c(iv)). These results suggest that the present system provides the ability to create highly complex multi-material 3D micro-structures that would be difficult or impossible to fabricate with existing 3D printing techniques. This unprecedented capability could enable various new applications such as multi-cellular tissue structure and vasculature, multi-functional 3D metamaterials, and micro-robotics.

3.6.2. Multi-particle-loaded 3D structure

Particle-loaded photocurable solutions have been employed in

Table 3
Printing parameters for the samples presented in this work.

Section	Sample	Materials	Light intensity (mW cm^{-2})	Layer thickness (μm)	Curing time (s)	Pumping time (s)
Cross-contamination (Sec.3.5)	Beams	PEGDA250 (0.8 μM $DiOC_2$) PEGDA250 (0.8 μM RhB)	10	100	1	3 ~ 11
Multi-material 3D micro-structures (Sec.3.6.1)	Taiji symbol	PEGDA250 (1 mM $DiOC_2$) PEGDA250 (1 mM RhB)	10	50	1.2	7
	Tensegrity	PEGDA250 (1 mM $DiOC_2$) PEGDA250 (1 mM RhB)	10	20	0.8	7
	Micro-capillary	PEGDA250 (1 mM $DiOC_2$) PEGDA250 (1 mM RhB)	10	20	0.8	7
Multi-particle-loaded structure (Sec.3.6.2)	Helix	PEGDA250 PEGDA250 (Cu) PEGDA250 (Al_2O_3)	10	50	1 1.2 1.2	11
	Taegeuk symbol	PEGDA250 (Cu) PEGDA250 (Al_2O_3)	10	25	700 300	90
Multi-responsive hydrogel structure (Sec.3.6.3)	Bilayer-beam	NIPAAm AA	30	30	10 0.5	7

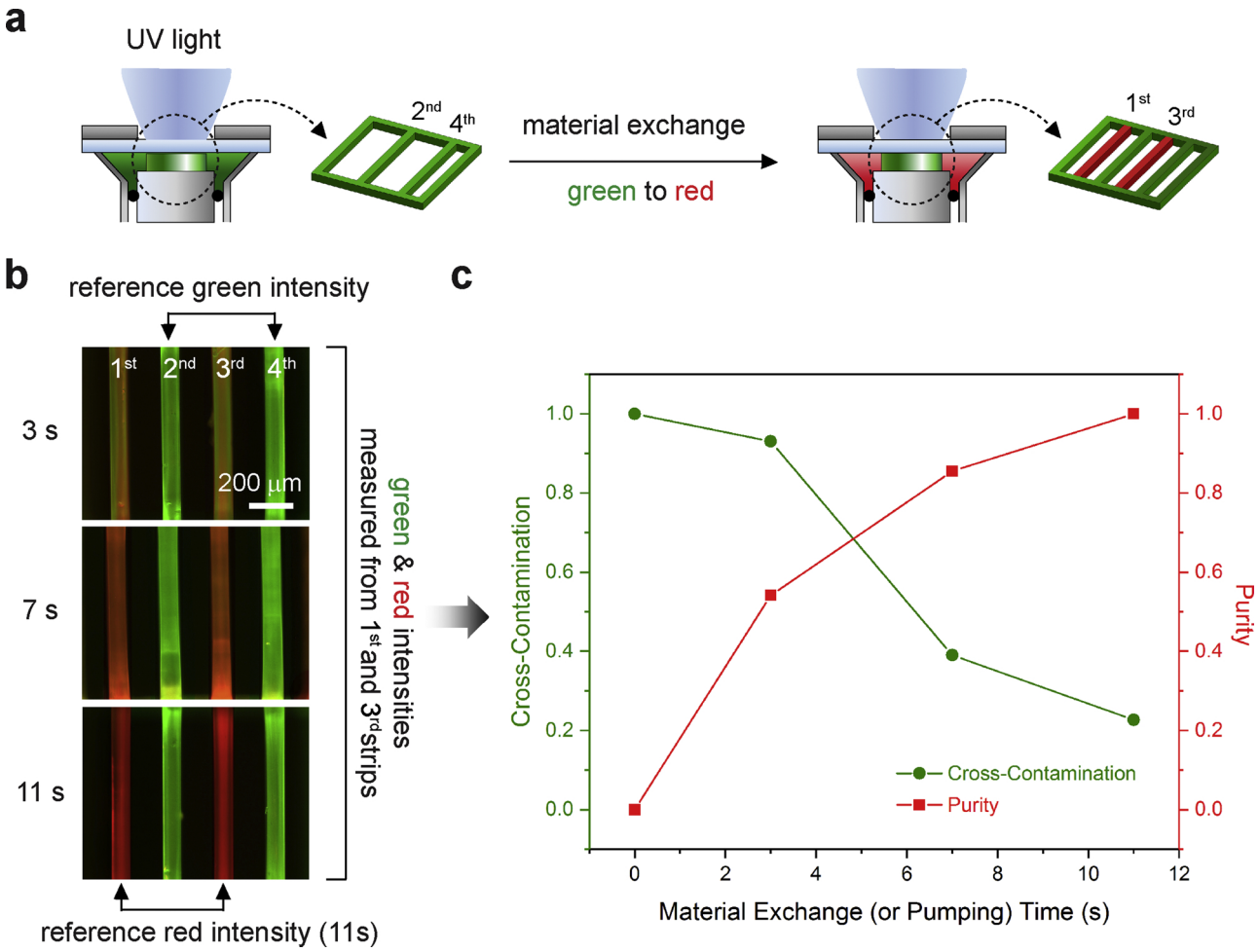

Fig. 3. Multi-material cross-contamination assessment. (a) Schematic illustration of the 3D printed test sample having four thin strips made of two different fluorescent materials. (b) Fluorescent microscope image of the test samples printed with different material exchange time (3, 7, or 11 s). (c) Progression of the two indices, Cross-contamination index (green circles) and Purity index (red squares), with pumping time. (For interpretation of the references to colour in this figure legend, the reader is referred to the web version of this article).

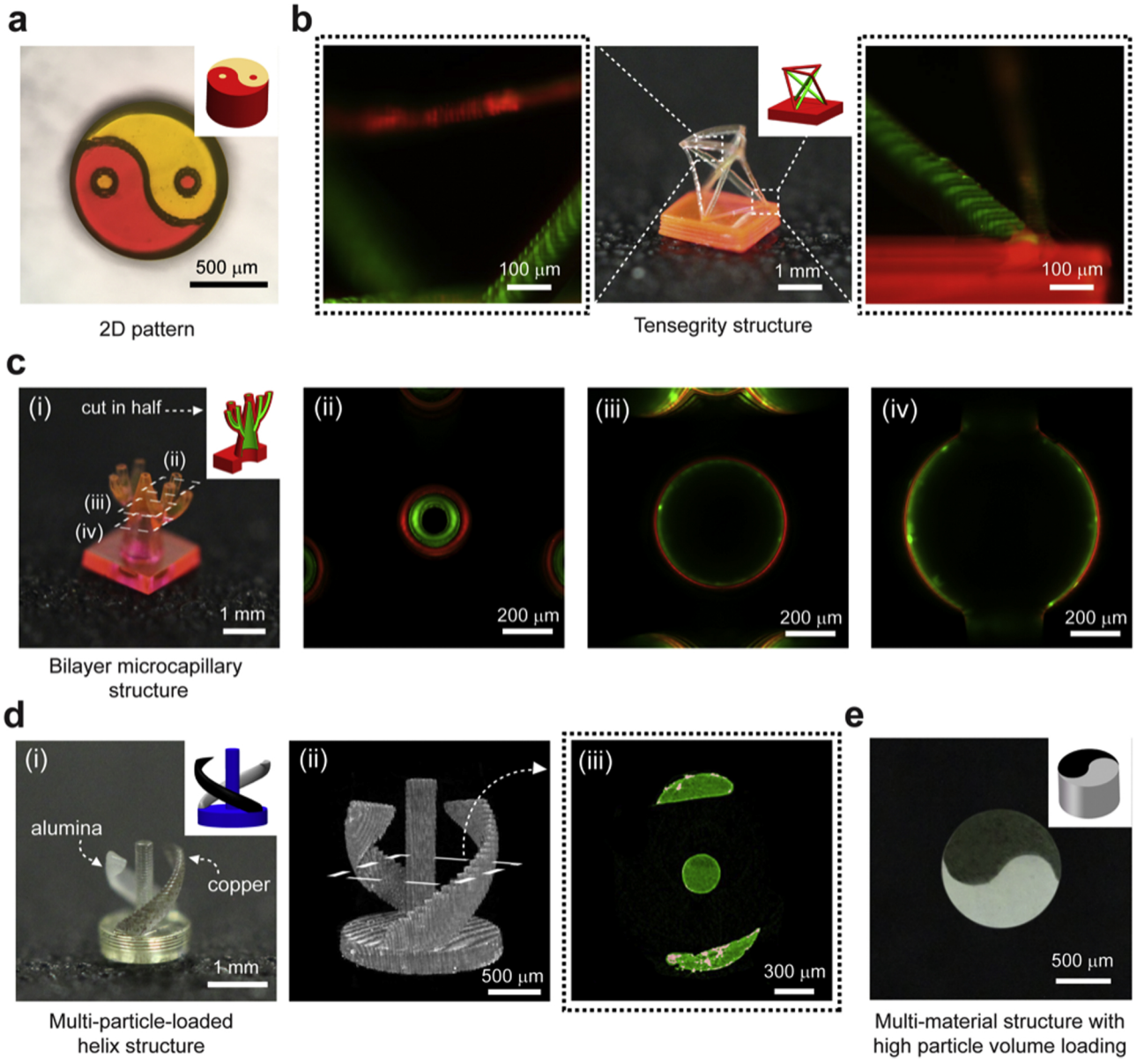

Fig. 4. Multi-material micro 3D structures fabricated with MM-PμSL. (a) Optical microscope image of the Taiji symbol patterned cylinder made of two different materials. (b) Fluoresecnet microscope images of the tensegrity structure consisting of multi-material high aspect ratio beams. (c) Confocal fluorescent microscope images in different parts of the multi-material bilayer micro-caplillary structure: top (ii), middle (iii), and bottom (iv). (d) 3D helix composed of three different parts; particle-free center pillar, two helix arms loaded with copper and alumina nano-particles. 3D (ii) and cross-sectional (iii) micro CT images of the structure. The green areas and white dots indicate the polymer matrix and particles, respectively. (e) Taegeuk symbol patterned cylinder with high particle loading (16 vol. %) of two different materials (copper and alumina nano-particles in black and white areas, respectively). (For interpretation of the references to colour in this figure legend, the reader is referred to the web version of this article).

stereolithography to extend properties and functionalities of a 3D printed object beyond those of photocurable polymers. Examples include metallic and ceramic 3D parts obtained through pyrolysis of a 3D printed particle-loaded polymers [15,41] and 3D tissue scaffolds printed from photopolymers with suspended living cells [21,49]. With the pressure-tight fluidic cell that allows for facile control of multiple flow streams, our MM-PμSL provides a unique platform to integrate various particles in a single 3D structure. To demonstrate this capability, we printed a 3D helix having 3 arms shown in Fig. 4d (i), with each arm made of different materials; particle-free center pillar (transparent), two helix arms loaded with copper (black) and alumina (white) nano-particles. Since the presence of particles increases the viscosity of a photopolymer (Appendix A. Fig. S5 and Table S2) [50], a longer pumping time of 11 s was used to ensure enough material influx during material exchange (Table 3). The height of the overall structure and the diameter of the arms are 2 mm and 300 μm, respectively. 3D (Fig. 4d (ii)) and cross-sectional image (Fig. 4d (iii)) of the structure were obtained by micro computed-tomography (micro CT). The green areas and white dots in Fig. 4d (iii) represent the polymer and nano-particles, respectively, confirming that the particles were selectively loaded in the desired parts. Also demonstrated is a multi-material 3D structure with high solid loading of nano-particles (Table 1), which could potentially be converted to a ceramic/metallic structure via thermal post-processing such as pyrolysis and sintering [41,51]. We printed a cylinder patterned with a Taeguek symbol consisting of two parts loaded with 16 vol. % of copper (black) and alumina (white) nano-particles, respectively, as shown in Fig. 4e. The diameter and height of the structure are 1 mm and 350 μm, respectively. A longer

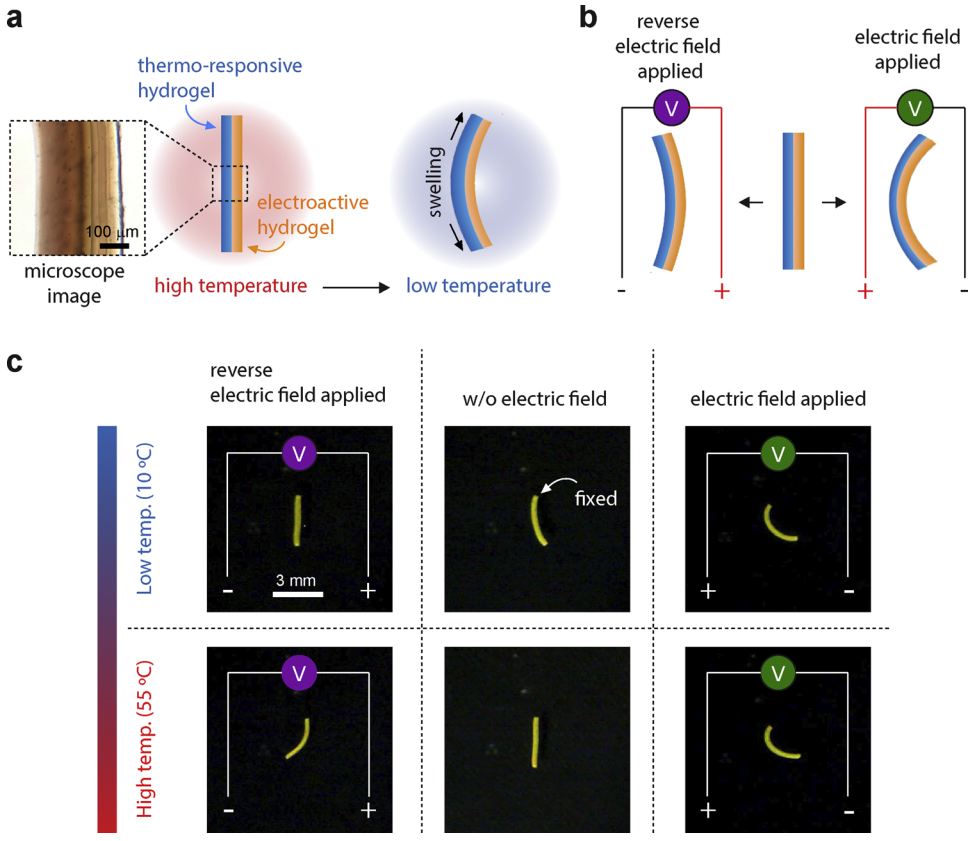

Fig. 5. Multi-responsive bilayer hydrogel beam printed with two different stimuli-responsive hydrogels; thermo-responsive and electroactive hydrogels. Schematic illustration of bending deformation of the bilayer beam according to temperature change (a) and electric field direction control (b). (c) Various modes and degrees of bending deformation of the structure in response to the combination of simultaneously applied stimuli.

pumping time of 90 s (Table 3) was used for material exchange because of higher viscosity (~ 270 cP) of the solutions (Appendix A. Fig. S5 and Table S2). These results suggest that MM-PμSL could potentially enable selective assembly of various non-photocurable functional materials including carbon nanotubes, graphene, quantum dots and even different cell lines.

3.6.3. *Multi-responsive hydrogel structure*

3D printing of stimuli-responsive hydrogels is on the rise of gaining growing attention for smart materials and structures for many applications including soft robotics, targeted drug delivery, and tissue engineering [52]. Multi-responsive 3D hydrogel fabricated by MM-PμSL will significantly extend the potential of smart structures by enabling more diverse and complex deformation in response to various stimuli simultaneously. Using MM-PμSL, we fabricated a bilayer beam with two different stimuli-responsive hydrogels; thermo-responsive [39] and electroactive [40] hydrogels (Fig. 5). Materials used to prepare the photocurable precursor solutions are listed in Table 1. The thermo-responsive hydrogel swells at a temperature below its low critical solution temperature (LCST) of 32 °C, and shrinks when the temperature is above its LCST [53]. Also, the electroactive hydrogel exhibits different degrees of swelling in an electrolyte when an electric field is applied [54]. The thickness of each hydrogel layer is 150 μm and the total length of the beam is 2.7 mm. The bilayer beam was straight at high temperature (55 °C) due to the same equilibrium swelling of the two hydrogels. However, when the temperature was lowered to 10 °C, only thermo-responsive hydrogel swelled further while electroactive hydrogel remained the same, causing the whole beam to bend, as illustrated in Fig. 5a. When this beam was subjected to an electric field, the electroactive hydrogel swelled or shrank depending on the direction of the electric field, again causing the whole beam to bend, as illustrated in Fig. 5b. In our experiments where we varied temperature (Appendix A. Fig. S6) and electric field directions (Appendix C. Video S2), the bilayer multi-responsive hydrogel beam showed various modes and degrees of bending deformation as expected, depending on the combination of simultaneously applied stimuli, as shown in Fig. 5c.

4. Conclusions

Stereolithography-based multi-material 3D printing methods reported thus far suffer from their long printing time due to interruptive and time-consuming material change processes for liquid-state materials in a vat. In this work, we presented a rapid multi-material micro 3D printing with a novel MM-PμSL system with an integrated fluidic cell in which multiple liquid photopolymers can be quickly exchanged through dynamic fluidic control. More than 95% of the material inside the fluidic cell can be exchanged within a few seconds, showing an order of magnitude faster performance than previously reported multi-material stereolithography techniques. Based on the system characterization results we obtained, we successfully demonstrated high-resolution 3D printing of multi-material structures. We also presented 3D printing of a multi-particle-loaded structure with embedded metal (copper) and ceramic (alumina) nano-particles. Also demonstrated was 3D printing of a multi-responsive hydrogel bilayer beam with thermo-responsive and electroactive hydrogels. All the multi-materials micro 3D structures presented herein were printed within less than an hour, showing remarkable improvement in manufacturing throughput while maintaining excellent micro-scale printing precision. A few limitations of the current system configurations to be addressed in future research include increasing material consumption with the number of materials used due to unavoidable material mixing during material change and compromised process throughput for highly viscous materials due to reduction in a material flow rate. Nevertheless, considering rapidly growing number of new printable materials with emerging properties, we believe our rapid multi-material micro 3D printing technique will become a new enabling manufacturing tool for facile production of multi-functional structures and devices across all fields.

Competing financial interests

The authors declare no competing financial interests.

Acknowledgements

The authors gratefully acknowledge the support from Rutgers University through the School of Engineering and the Department of Mechanical and Aerospace Engineering, Defense Acquisition Program Administration and Agency for Defense Development (UD150032GD), and Haythornthwaite Foundation Research Ignition Grant. The authors also thank Bernd Geh and Carl Zeiss for the generous donation of the h-line lithography lens used in this work.

Appendix A. Supplementary data

Supplementary material related to this article can be found, in the online version, at doi:https://doi.org/10.1016/j.addma.2019.03.031.

References

[1] D.L. Bourell, J.J. Beaman, M.C. Leu, D.W. Rosen, A brief history of additive manufacturing and the 2009 roadmap for additive manufacturing: looking back and looking ahead, Proceedings of RapidTech, (2009), pp. 24–25.
[2] J.A. Lewis, Direct ink writing of 3D functional materials, Adv. Funct. Mater. 16 (17) (2006) 2193–2204.
[3] J.A. Lewis, G.M. Gratson, Direct writing in three dimensions, Mater. Today 7 (7-8) (2004) 32–39.
[4] O.A. Mohamed, S.H. Masood, J.L. Bhowmik, Optimization of fused deposition modeling process parameters: a review of current research and future prospects, Adv. Manuf. 3 (1) (2015) 42–53.
[5] B.J. De Gans, P.C. Duineveld, U.S. Schubert, Inkjet printing of polymers: state of the art and future developments, Adv. Mater. 16 (3) (2004) 203–213.
[6] H. Kodama, Automatic method for fabricating a three-dimensional plastic model with photo-hardening polymer, Rev. Sci. Instrum. 52 (11) (1981) 1770–1773.
[7] C.W. Hull, Apparatus for production of three-dimensional objects by stereolithography, Google Patents, 1986.
[8] S. Maruo, O. Nakamura, S. Kawata, Three-dimensional microfabrication with two-photon-absorbed photopolymerization, Opt. Lett. 22 (2) (1997) 132–134.
[9] B.H. Cumpston, S.P. Ananthavel, S. Barlow, D.L. Dyer, J.E. Ehrlich, L.L. Erskine, A.A. Heikal, S.M. Kuebler, I.-Y.S. Lee, D. McCord-Maughon, Two-photon polymerization initiators for three-dimensional optical data storage and microfabrication, Nature 398 (6722) (1999) 51.
[10] J.W. Stansbury, M.J. Idacavage, 3D printing with polymers: challenges among expanding options and opportunities, Dent. Mater. 32 (1) (2016) 54–64.
[11] W.E. Frazier, Metal additive manufacturing: a review, J. Mater. Eng. Perform. 23 (6) (2014) 1917–1928.
[12] H. Seitz, W. Rieder, S. Irsen, B. Leukers, C. Tille, Three-dimensional printing of porous ceramic scaffolds for bone tissue engineering, J. Biomed. Mater. Res. Part B: Appl. Biomater. 74 (2) (2005) 782–788.
[13] D. Isakov, Q. Lei, F. Castles, C. Stevens, C. Grovenor, P. Grant, 3D printed anisotropic dielectric composite with meta-material features, Mater. Des. 93 (2016) 423–430.
[14] H.N. Chia, B.M. Wu, Recent advances in 3D printing of biomaterials, J. Biol. Eng. 9 (1) (2015) 4.
[15] Q. Wang, J.A. Jackson, Q. Ge, J.B. Hopkins, C.M. Spadaccini, N.X. Fang, Lightweight mechanical metamaterials with tunable negative thermal expansion, Phys. Rev. Lett. 117 (17) (2016) 175901.
[16] S. Babaee, J. Shim, J.C. Weaver, E.R. Chen, N. Patel, K. Bertoldi, 3D soft metamaterials with negative Poisson's ratio, Adv. Mater. 25 (36) (2013) 5044–5049.
[17] C.L. Ventola, Medical applications for 3D printing: current and projected uses, Pharm. Ther. 39 (10) (2014) 704.
[18] J.A. Lewis, B.Y. Ahn, Device fabrication: three-dimensional printed electronics, Nature 518 (7537) (2015) 42.
[19] S. Bose, S. Vahabzadeh, A. Bandyopadhyay, Bone tissue engineering using 3D printing, Mater. Today 16 (12) (2013) 496–504.
[20] S.M. Peltola, F.P. Melchels, D.W. Grijpma, M. Kellomäki, A review of rapid prototyping techniques for tissue engineering purposes, Ann. Med. 40 (4) (2008) 268–280.
[21] D.B. Kolesky, R.L. Truby, A.S. Gladman, T.A. Busbee, K.A. Homan, J.A. Lewis, 3D bioprinting of vascularized, heterogeneous cell-laden tissue constructs, Adv. Mater. 26 (19) (2014) 3124–3130.
[22] S. Khalil, J. Nam, W. Sun, Multi-nozzle deposition for construction of 3D biopolymer tissue scaffolds, Rapid Prototyp. J. 11 (1) (2005) 9–17.
[23] D. Kokkinis, M. Schaffner, A.R. Studart, Multimaterial magnetically assisted 3D printing of composite materials, Nat. Commun. 6 (2015) 8643.
[24] D. Espalin, J. Alberto Ramirez, F. Medina, R. Wicker, Multi-material, multi-technology FDM: exploring build process variations, Rapid Prototyp. J. 20 (3) (2014) 236–244.
[25] R. Melnikova, A. Ehrmann, K. Finsterbusch, 3D printing of textile-based structures by fused deposition modelling (FDM) with different polymer materials, IOP Conference Series: Materials Science and Engineering (2014) 012018.
[26] K. Wang, C. Wu, Z. Qian, C. Zhang, B. Wang, M.A. Vannan, Dual-material 3D printed metamaterials with tunable mechanical properties for patient-specific tissue-mimicking phantoms, Addit. Manuf. 12 (2016) 31–37.
[27] Z. Ding, C. Yuan, X. Peng, T. Wang, H.J. Qi, M.L. Dunn, Direct 4D printing via active composite materials, Sci. Adv. 3 (4) (2017) e1602890.
[28] X. Mu, T. Bertron, C. Dunn, H. Qiao, J. Wu, Z. Zhao, C. Saldana, H. Qi, Porous polymeric materials by 3D printing of photocurable resin, Mater. Horiz. 4 (3) (2017) 442–449.
[29] Q. Mu, L. Wang, C.K. Dunn, X. Kuang, F. Duan, Z. Zhang, H.J. Qi, T. Wang, Digital light processing 3D printing of conductive complex structures, Addit. Manuf. 18 (2017) 74–83.
[30] Q. Ge, A.H. Sakhaei, H. Lee, C.K. Dunn, N.X. Fang, M.L. Dunn, Multimaterial 4D printing with tailorable shape memory polymers, Sci. Rep. 6 (2016) 31110.
[31] Y. Lu, S.N. Mantha, D.C. Crowder, S. Chinchilla, K.N. Shah, Y.H. Yun, R.B. Wicker, J.-W. Choi, Microstereolithography and characterization of poly (propylene fumarate)-based drug-loaded microneedle arrays, Biofabrication 7 (4) (2015) 045001.
[32] C. Zhou, Y. Chen, Z. Yang, B. Khoshnevis, Digital material fabrication using mask-image-projection-based stereolithography, Rapid Prototyp. J. 19 (3) (2013) 153–165.
[33] C. Zhou, Y. Chen, Z. Yang, B. Khoshnevis, Development of multi-material mask-image-projection-based stereolithography for the fabrication of digital materials, Annual Solid Freeform Fabrication Symposium (2011).
[34] H. Yun, H. Kim, Development of DMD-based micro-stereolithography apparatus for biodegradable multi-material micro-needle fabrication, J. Mech. Sci. Technol. 27 (10) (2013) 2973–2978.
[35] C. Sun, N. Fang, D. Wu, X. Zhang, Projection micro-stereolithography using digital micro-mirror dynamic mask, Sens. Actuators A Phys. 121 (1) (2005) 113–120.
[36] X. Zheng, J. Deotte, M.P. Alonso, G.R. Farquar, T.H. Weisgraber, S. Gemberling, H. Lee, N. Fang, C.M. Spadaccini, Design and optimization of a light-emitting diode projection micro-stereolithography three-dimensional manufacturing system, Rev. Sci. Instrum. 83 (12) (2012) 125001.
[37] H. Lee, C. Xia, N.X. Fang, First jump of microgel; actuation speed enhancement by elastic instability, Soft Matter 6 (18) (2010) 4342–4345.
[38] H. Lee, J. Zhang, H. Jiang, N.X. Fang, Prescribed pattern transformation in swelling gel tubes by elastic instability, Phys. Rev. Lett. 108 (21) (2012) 214304.
[39] D. Han, Z. Lu, S.A. Chester, H. Lee, Micro 3D printing of a temperature-responsive hydrogel using projection micro-stereolithography, Sci. Rep. 8 (1) (2018) 1963.
[40] D. Han, C. Farino, C. Yang, T. Scott, D. Browe, W. Choi, J.W. Freeman, H. Lee, Soft robotic manipulation and locomotion with a 3D printed electroactive hydrogel, ACS Appl. Mater. Interfaces (2018).
[41] X. Zheng, H. Lee, T.H. Weisgraber, M. Shusteff, J. DeOtte, E.B. Duoss, J.D. Kuntz, M.M. Biener, Q. Ge, J.A. Jackson, Ultralight, ultrastiff mechanical metamaterials, Science 344 (6190) (2014) 1373–1377.
[42] Y.Y.C. Choong, S. Maleksaeedi, H. Eng, P.-C. Su, J. Wei, Curing characteristics of shape memory polymers in 3D projection and laser stereolithography, Virtual Phys. Prototyp. 12 (1) (2017) 77–84.
[43] R. Raman, B. Bhaduri, M. Mir, A. Shkumatov, M.K. Lee, G. Popescu, H. Kong, R. Bashir, High-resolution projection microstereolithography for patterning of neovasculature, Adv. Healthc. Mater. 5 (5) (2016) 610–619.
[44] H. Cui, R. Hensleigh, H. Chen, X. Zheng, Additive Manufacturing and size-dependent mechanical properties of three-dimensional microarchitected, high-temperature ceramic metamaterials, J. Mater. Res. 33 (3) (2018) 360–371.
[45] J.R. Tumbleston, D. Shirvanyants, N. Ermoshkin, R. Janusziewicz, A.R. Johnson, D. Kelly, K. Chen, R. Pinschmidt, J.P. Rolland, A. Ermoshkin, Continuous liquid interface production of 3D objects, Science (2015) aaa2397.
[46] D. Dendukuri, S.S. Gu, D.C. Pregibon, T.A. Hatton, P.S. Doyle, Stop-flow lithography in a microfluidic device, Lab Chip 7 (7) (2007) 818–828.
[47] F.M. White, Fluid Mechanics, McGraw-hill, 1986.
[48] I. Gibson, D. Rosen, B. Stucker, Additive Manufacturing–3D Printing, Rapid Prototyping, and Direct Digital Manufacturing, Springer, New York, 2015.
[49] S.V. Murphy, A. Atala, 3D bioprinting of tissues and organs, Nat. Biotechnol. 32 (8) (2014) 773.
[50] M. Mooney, The viscosity of a concentrated suspension of spherical particles, J. Colloid Sci. 6 (2) (1951) 162–170.
[51] J.W. Lee, I.H. Lee, D.-W. Cho, Development of micro-stereolithography technology using metal powder, Microelectron. Eng. 83 (4-9) (2006) 1253–1256.
[52] M.A.C. Stuart, W.T. Huck, J. Genzer, M. Müller, C. Ober, M. Stamm, G.B. Sukhorukov, I. Szleifer, V.V. Tsukruk, M. Urban, Emerging applications of stimuli-responsive polymer materials, Nat. Mater. 9 (2) (2010) 101.
[53] C. Wu, X. Wang, Globule-to-coil transition of a single homopolymer chain in solution, Phys. Rev. Lett. 80 (18) (1998) 4092.
[54] T. Shiga, T. Kurauchi, Deformation of polyelectrolyte gels under the influence of electric field, J. Appl. Polym. Sci. 39 (11-12) (1990) 2305–2320.